Article

Motion Intention Estimation for Active Power-Assist Lower Limb Exoskeleton Robot (APAL)

Mantian Li [1,2], Jing Deng [1], Fusheng Zha [1,2,*], Shiyin Qiu [1], and Xin Wang [2]

[1] State Key Laboratory of Robotics and System, Harbin Institute of Technology (HIT), Harbin 150001, China; Emails: limt@hit.edu.cn (M.L.); stdr_dj@163.com (J.D.); zhafusheng@hit.edu.cn (F.Z.); qsy@hit.edu.cn (S.Q.).
[2] Shenzhen Academy of Aerospace Technology, Shenzhen 518000, China; Email: xin.wang@chinasaat.com (X.W.).
* Corresponding author: zhafusheng@hit.edu.cn; Tel.: +86-0451-86414174

Abstract: The active power-assist function greatly expands the potential applications of exoskeleton robots, yet the motion intention estimation (MIE) for active power-assist strategy is quite problematic. Through the analysis of the conduction path and the different stage manifestations of motion intention in human body, we confirmed that the joint torque of human body meets the basic requirements of MIE for the active power-assist that we suggest, namely: (i) it reflects the direction and intensity of the wearer's efforts; (ii) it precedes the human limb motion; (iii) it generates real-time and continuous output. Thus, an online calculation method of human joint torque was proposed. The sensing system integrated in exoskeleton robots was designed to perceive motion data and foot contact force of a human body. A special inverse dynamics with a parameterized model of the human body was proposed. Contrast experiments were carried out with the motion capture system, which results' accuracy and similarity were evaluated via the root mean square error and correlation coefficient. The comparative analysis of two synchronous results shows good accuracy of the proposed MIE method, which lays the foundation for the realization of active power-assist.

Keywords: motion intention estimation; active power-assist; exoskeleton robot; inverse dynamics.

1. Introduction

The active power-assist function can greatly expands the potential applications of exoskeleton robots by expanding physical capability of human body, such as enabling amyotrophic patients to regain walking ability, helping the elderly to climb stairs, and enhancing soldiers to exceed their physical limits, i.e., run faster and jump higher. The motion of a human body is complicated and has strong randomness, and the recognition of the human motion intentions is always confusing. To realize active power-assist, the exoskeleton needs to prejudge the wearer's intention and actively assist the limb motion of the human body, which poses new challenges to the motion intention estimation (MIE) technology.

MIE can be seen as a particular way for the robot to obtain the operators' instructions. The conventional machine reads the operator's instructions through a human-machine interface such as a keyboard or buttons. Assistive exoskeleton for paraplegic patients such as ReWalk [1], EKSO [2], i.e. also use buttons on the cane to input some simple and discrete upper-level instructions, such as stand up, sit down, walk along, etc., while the lower-level instructions such as joints' movement are taken over by the exoskeleton. This kind of simple approach is accessible for handicapped person, but it limits the wearer's flexibility and is hard to adapt to the complex environment.

Supporting arbitrary motion of the wear is our first concern on MIE method. Coordination with wearer's joints movement instead of replacing them is more likely for an exoskeleton robot to support random movement of the wearer. The technology of directly manipulating a robot through the human limb movement has been elaborated and brought significant benefits to the teleoperation and minimally invasive surgery [3]. There are several ways to extract motion intentions. The sensitivity

 doi:10.20944/preprints201806.0149.v1

amplification control (SAC) method [4] proposed at the UC Berkeley and implemented in BLEEX exoskeleton is widely studied. The dynamic feedforward compensation [5] makes the BLEEX transparent to external force, which, thus, spontaneously follows the human body. The human-machine movement deviation (HMMD)-based MIE is used in the upper limb ULERD [6] and load-carrying PRMI [7] exoskeletons. The attitude deviations are detected and transferred into joints velocity or torque command for the exoskeleton to catch up. The human-machine contact force (HMCF)-based MIE seems better [8, 9], because it is less likely to cause asynchronies and motion interference. Man-machine interaction force indicates the direction and speed of the human body, which reduces the task for the exoskeleton to tracking of the human body with impedance control or other strategies. The above SAC, HMMD, and HMCF are MIE methods for follow-up strategies whose significant drawback is that the exoskeleton will not actively overtake the wearer's efforts to drag his/her limbs towards the desired direction.

Actively assisting the human body is our second concern on MIE. The exoskeleton robot should not just follow, but estimate the wearer's needs and take the initiative to assist. The Hybrid Assistive Limb (HAL) built by Cyberdyne Inc., Tsukuba, Japan, is a typical active power-assist type [10]. They use muscle activity to represent the wearer's motion intention, and major breakthrough was made. The muscle activity was estimated from electromyography (EMG) signals and convert into the wearer's joints torque, then the HAL generate power assist torque by amplifying the wearer's own joint torque. Many other exoskeletons with EMG method also confirm that the muscle activity based MIE is suitable for realizing active power-assist function [11-13]. There are also other methods for estimating the muscle activity, e.g., the muscle stiffness method [14]. However, it is not easy to calculate joint torque from EMG signals, because there are many imprecise physical models between the EMG signals and the joint torques, such as the muscle force versus EMG signal, moment arm of the muscle versus angle of the joint, and the redundancy induced by the multiple muscles driving the same joint, etc. [15]. All this results in increasing complexity and uncertainty in actual implementation.

The above brief survey of MIEs for different type of exoskeletons indicates that human motion intention can be tracked in multiple different ways. The original keyboard-and-buttons-based MIE limit user's flexibility. The SAC, HMMD and HMCF methods extract human intention form the wearer's limb motion, man-machine attitude deviations and interaction force, which can support arbitrary motion of human body, but are limited to follow-up strategy. The active power-assist function was successfully realized with the muscle-activity-based MIE, yet the complexity and uncertainty limit its application.

This paper discusses the MIE method for the active power-assist lower limb (APAL) exoskeleton robot. We first analyzed the manifestations of human motion intention in different stage, then, critically choose the joint torque to be the motion intention, and briefly explained its effectiveness for the active power-assist function. The rest main problem is the accurate estimation of the wearer's joint torque. A parameterized model of the human body is established and inverse dynamics specially solved. A sensor system integrated in the exoskeleton structure is designed to detect movement and posture of the human body, and a pair of special shoes are developed to measure the wearer's foot contact force. With all these sensor signals, joint torque of the human lower limbs was calculated on line. Contrast experiments were carried out with a motion capture system to evaluate the accuracy of the newly proposed sensor system and algorithm.

2. Materials and Methods

2.1. Definition of motion intention

The motion intentions arising from the brain are converted into nerve impulses by the central nervous system and control the coordinate motion of muscle groups. The nerve impulses transfer along the nerve fibers to the muscle cells, causing the muscle contraction, thereby pulling the adjacent bones to generate joint torques, and driving the limbs to form the body movement. Finally, the limbs interact with environment to generate contact forces [16], as shown in Figure 1. It can be seen that the

Preprints (www.preprints.org) | NOT PEER-REVIEWED | Posted: 11 June 2018 doi:10.20944/preprints201806.0149.v1

motion intention has different forms at different stages from its generation to the manifestation. The motion intention can be represented from different aspects by EEG, nerve impulse, EMG, muscle force, joint torque, limb motion, limb posture, and contact forces. However, not any of these signals that can be extracted satisfies the conditions, which are required for the accurate interpretation of the motion intention and further realization of the active power-assist strategy. The appropriate MIE should have the following features:

1) Reflects the direction and intensity of the wearer's efforts;

2) Precedes the human limb motion;

3) Generates real-time and continuous output.

Correct direction helps prevent counteraction, while liner response to the effort intensity is essential for soft contact and cooperative movement. Precede the human limb motions to actively pull the human body to achieve the power-assist. Real-time and continuity features enable the controller to generate real-time instructions.

The intention for active power-assist is no longer an upper-level command, such as stand up or sit down, but a series of real-time and specific control instructions to each dynamic joints. Similarly, a cab passenger intention to travel from the foot of the mountain to the top implies no straightforward realization of the "drive up the hill" macro-command. Instead, the cab driver (or self-driving car system) must control the car direction, throttle and brake on each ramp, and make all the required turns.

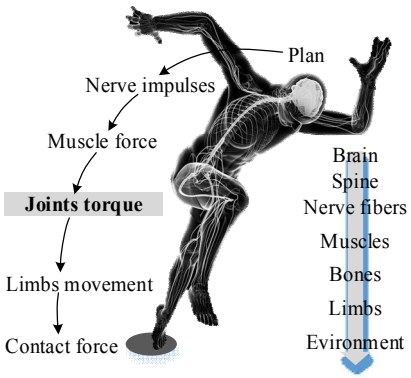

Figure 1. The transfer link and manifestation of motion intention

In the entire conduction chain of the motion intention, the limb movement and contact force are more accessible but less informative than the joints' torque. For example, when a person under study generates a muscle torque to stretch the knee joint, the knee will extend with acceleration, or contract with deceleration, or just stay still to maintain a half squat posture. From the detected movement of the knee joint, the observer cannot judge the direction of the person's motion intention, in contrast to the joint torque, which exactly fits the above four requirements. Firstly, the sign of the joint torque represents the effort's direction. Secondly, the magnitude of the joint torque linearly reflects the effort intensity. Thirdly, it is well-known that force causes the acceleration of an object, and its trajectory is obtained by the double integration of the acceleration, so the joint torque is always ahead of the limb trajectory. Finally, the joint torque continuously reflects the wearer's motion intention in the real time scale. Medical data show that the nerve impulse from the central nervous system reaches the muscle contraction in about 10ms [17]. Meanwhile, the bandwidth of the human lower limb is less than 5Hz [18], which implies the system delay of 250ms. It is 25 times higher than that of the nerve impulse reaching the joint torque. Therefore, the latter delay is negligible, while the joint torque is chosen to represent the wearer's motion intention, insofar as it meets the above requirements of active power-assist.

2.2. The active power-assist mechanism

Assuming that the exoskeleton robot acquires the data on its wearer's joint torque in real-time, and exerts a fully equivalent torque on the human body, the wearer will need little effort to move

Preprints (www.preprints.org) | NOT PEER-REVIEWED | Posted: 11 June 2018 doi:10.20944/preprints201806.0149.v1

his/her limbs. This is the origin of the proposed active power-assist method. It provides the muscular torque proportional compensation (MTPC), which allows the human body to maintain its posture and state of motion through the exoskeleton robot. This method (hereinafter referred to as MTPC method) has the following mathematical description:

$$\begin{cases} \tau = \tau_H + \tau_E \\ \tau_E = \alpha\tau, \ (0 \le \alpha \le 1) \end{cases} \tag{1}$$

where τ is the required torque for the human body, τ_H is the muscular torque generated by human muscles, τ_E is the auxiliary torque from the exoskeleton, and α is the assistive factor. Noteworthy is that no exoskeleton is expected to completely replace muscles of the human body, because human skin cannot bear excessive loads. Therefore, the assistive factor is selected in the range from 0 to 0.25 [19]. Here, we briefly attest the active power-assist strategy in the aspect of the reduction of power and torque amplitude.

Assume that *P* is the total power required by the joint for completing a particular action. When the exoskeleton assists the human body to perform the same action, the total power should remain unchanged. This yields

$$P = \tau\omega = P_H + P_E = \tau_H\omega + \tau_E\omega \tag{2}$$

where P_H is human muscle power, P_E is the exoskeleton power, and ω is joint angular velocity. Substitution of Equation 2 into Equation 1 yields

$$\begin{cases} |\tau_H| = |1-\alpha| \cdot |\tau| \le |\tau| \\ |P_H| = |1-\alpha| \cdot |P| \le |P| \end{cases} \tag{3}$$

It can be seen that the MTPC method can reduce both the amplitude of the joint torque and the power consumption of the human body, which theoretically realizes the active power-assist functionality. Moreover, there is no need for this method to distinguish the forms of motion, such as forward or backward ones, accelerating or decelerating, walking, running, jumping, or other. This is a general method, which seems to very lucrative for the support of arbitrary movements of the human body.

The architecture of active power-assist loop is shown in Figure 2. In such a human-machine coupled system, there are two controllers, one is the human brain, and the other is the CPU of the exoskeleton robot. The role of the human brain is to sense the actual movement of the body through the cochlea/inner ear, vision, touch, and so on, and to emit the nerve impulses to drive the body toward the desired state; the role of the exoskeleton robot is to assist the human body. Therefore, a kinematics relationship with the human body is firstly established based on the man-machine coupling mechanism, then the motion data and interaction force of the wearer will be measured by the integrated sensing system in the structure. These signals are substituted into a kinetic equation of the human dynamic model to calculate the required torque τ (which is defined as the motion intention). Next, the value of τ is multiplied by the assistive factor and exerted to the respective joint, in order to reduce the joint torque contribution of the human body.

Preprints (www.preprints.org) | NOT PEER-REVIEWED | Posted: 11 June 2018 doi:10.20944/preprints201806.0149.v1

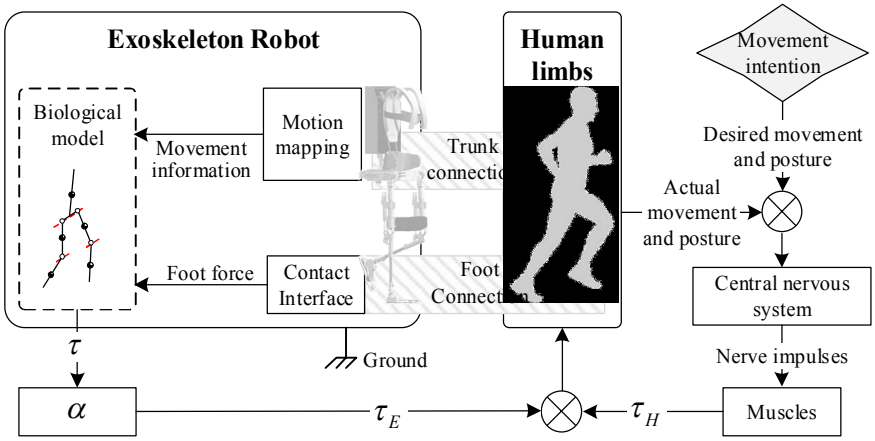

Figure 2. Architecture of active power-assist loop

This architecture has several notable features:

1) The wearer has an absolute control, since the exoskeleton interaction with the human body is reduced to the auxiliary torque with a preset assistive factor, which does not force the wearer to move at a set speed or trajectory;

2) The time delay of the MIE algorithm is very short. As soon as human muscles contract and exert the acceleration to body limbs, the exoskeleton detects the change immediately and issues control commands after one sampling period (1ms for APAL);

3) It provides a spontaneous active assist mechanism for exoskeleton robots without any additional constraints;

4) There is no need for the power-assist exoskeleton robot to distinguish any motion patterns of the human body, which means it can support arbitrary motions of its wearer.

2.3. The muscular torque assessment

Human joint torque is difficult to measure, but it can be assessed indirectly by analyzing other signals. Within framework of the Newtonian mechanics, the motion of a multi-rigid-body system can be deduced from the external forces acting on it and vice versa. This notion holds for the human body motion. The inverse dynamics approach (IDA) has been widely used in clinical data analysis (CGA) [20]. The trajectories of each joint and ground reaction forces (GRF) are obtained by the motion capture system with a three-dimensional force plate [21]. Then, the torque of each joint can be calculated using an inverse dynamic model of a human body (also referred to as the Helen Hayes model). However, the available motion capture systems are quite cumbersome and not portable, so the integrated and simplified sensing system for the exoskeleton robot was designed and implemented in this study.

2.3.1. Simplified human dynamic model

IDA is based on the parametric model of a human body. We use a simplified model to study the motion only in the sagittal plane. A human body is simulated by a 5-bar dynamic model, which treats the pelvis and upper body parts (including the trunk, arm, and head) as a single component *B*. Right and left thighs are reduced to component T, while the respective (right and left) shank and foot are combined into a single component S. The body coordinate system is fixed to component B, and its origin is set at the midpoint between two hip joints, as shown in Figure 3.

Preprints (www.preprints.org) | NOT PEER-REVIEWED | Posted: 11 June 2018 doi:10.20944/preprints201806.0149.v1

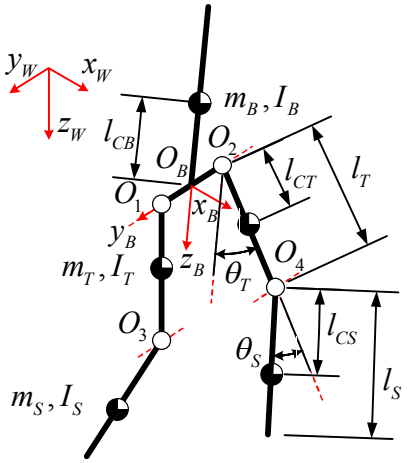

Figure 3. Parametric model of a human body used in this study

where m_B, m_T, and m_S are the masses of components B, T, and S, respectively; I_B, I_T and I_S are the rotational inertia at their mass center on the coordinate axis y_B; l_T and l_S are length of thigh and shank, respectively; l_{CB}, l_{CT}, and l_{CS} are distances from the mass centers of B, T, and S, respectively, to the coordinate origin O_B, hip joint, and knee joint, respectively. There are many relevant discussions on the calculation of body dimensions and inertial parameters [22]. In this study, a male subject of 75kg weight and 1.75m height is used as an example. The respective parameters are listed in Table 1.

Table 1. Parameters of the simplified human dynamic model.

m_T (kg)	m_S (kg)	I_T ($\mathrm{kg \cdot mm^2}$)	I_S ($\mathrm{kg \cdot mm^2}$)	l_T (mm)	l_S (mm)	l_{CT} (mm)	l_{CS} (mm)
9.69	5.21	1.39×10^5	1.03×10^5	424	422	187	217

2.3.2. Inverse dynamics

Human walking process includes several states, which can be reduced to (i) single support, (ii) double support, and (iii) double off-the-ground position. Given a variety of restraints on the feet at different states, the dynamic models are also different. Commonly, it is necessary to introduce a finite-state-machine (FSM) to select the dynamic equations corresponding to the respective states. However, such switching of dynamic equations can provide discontinuous and biased outputs, leading to the motion control instability. Moreover, slight sensing errors made in some non-relevant joints may cause drastic fluctuations to the multi-body inverse dynamics. For example, the angle fluctuations of the supporting ankle may cause a high acceleration of the trunk, and noise signals will submerge the curves of joint torques. To solve the above problems, we transform the integral inverse dynamics of the whole body into that of two separate legs, thereby shortening the kinematic chain and reducing some local disturbances. Then, according to the linear superposition principle of force acting on the rigid-body system, the inverse dynamics of a single leg is further factorized into the mass-induced joint torques and foot contact force (FCF)-induced joint torques.

Preprints (www.preprints.org) | NOT PEER-REVIEWED | Posted: 11 June 2018 doi:10.20944/preprints201806.0149.v1

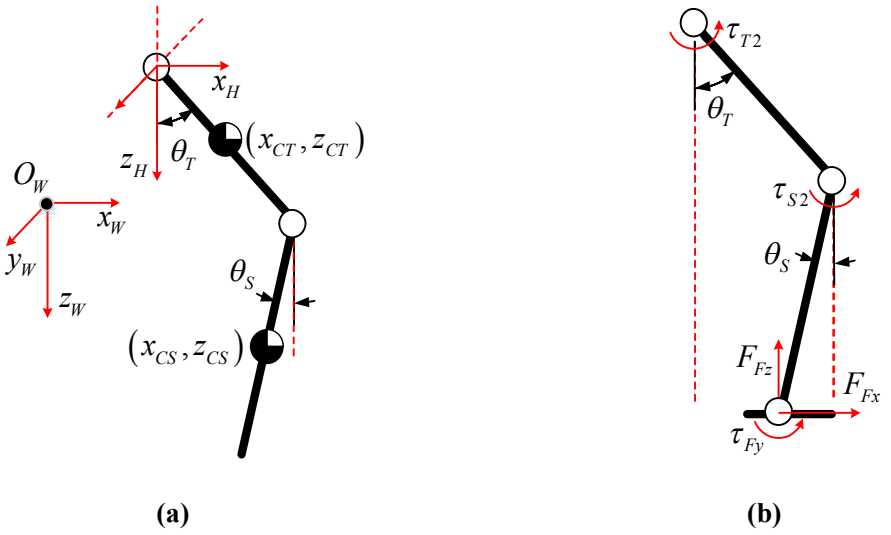

(a) **(b)**

Figure 4. Simplified dynamic model of a single leg. **(a)** Model to determine joint torque induced by mass forces; **(b)** Model to calculate joint torque induced by foot contact forces.

In the calculations of mass-induced joint torques, the foot contact force is neglected, and the leg is considered to be suspended to component *B* by the hip joint, where the coordinate origin is set, as shown in Figure 4(a). This is a two-bar dynamic model with floating pedestals. The Lagrange method is used to solve the inverse dynamics via Equation 4. More details on the calculation of kinetic energy *K* and potential energy *P* are given in Appendix A.

$$\begin{cases} \tau_{T1} = \dfrac{\mathrm{d}}{\mathrm{d}t}\left[\dfrac{\partial(K-P)}{\partial\dot{\theta}_T}\right] - \dfrac{\partial(K-P)}{\partial\theta_T} \\ \tau_{S1} = \dfrac{\mathrm{d}}{\mathrm{d}t}\left[\dfrac{\partial(K-P)}{\partial\dot{\theta}_S}\right] - \dfrac{\partial(K-P)}{\partial\theta_S} \end{cases} \tag{4}$$

In the estimation of FCF-induced joint torques, the foot end touches the ground while the upper end of the leg supports the entire trunk. Ignoring the mass, we can calculate the joint torque via the static equilibrium equation, as shown in Figure 4(b). FCF values, including F_{Fx}, F_{Fz} and τ_{Fy}, are measured, and the force balance equations are solved to derive the hip τ_{T2} and knee τ_{S2} joint torques

$$\begin{cases} \tau_{T2} = F_{Fx}(l_T\cos\theta_T + l_S\cos\theta_S) + F_{Fz}(l_T\sin\theta_T - l_S\sin\theta_S) + \tau_{Fy} \\ \tau_{S2} = F_{Fx}l_S\cos\theta_S - F_{Fz}l_S\sin\theta_S + \tau_{Fy} \end{cases} \tag{5}$$

Finally, the mass- and FCF-induced joint torques are summed to obtain the total joint torque of the hip and knee.

$$\begin{cases} \tau_T = \tau_{T1} + \tau_{T2} \\ \tau_S = \tau_{S1} + \tau_{S2} \end{cases} \tag{6}$$

3. Sensor system design

The sensor system is designed to measure all signals required for solving IDA equation. The motion capture system is instrumental in the analysis of human body motion, yet its subject has to stay in a limited area. Once the camera or force plate ranges are exceeded, or the marker points on the subject are covered, the outputs will be invalid. We cannot rely on the motion capture system to provide motion data for controlling the exoskeleton. Instead, we have to design a new sensing system to meet the requirement of portability and simplicity.

Preprints (www.preprints.org) | NOT PEER-REVIEWED | Posted: 11 June 2018 doi:10.20944/preprints201806.0149.v1

According to Equations 4 and 5, the required data include the trunk (component B) posture, acceleration of hip joints, and foot contact forces (FCF). To avoid misalignment of the sensor and wearer's discomfort, no direct measurements from a human body are used. Instead, the entire sensor system is integrated into the exoskeleton structure to measure the motion information of the exoskeleton, and then, according to the man-machine motion mapping, the human body motion data are derived. The motion mapping is ensured by the structural design, which description can be found elsewhere [23] and is omitted here for brevity. The composition of the sensor system is described below.

3.1. Overall hardware architecture

The central controller is B&R PLC (Programmable Logic Controller by B&R Industrial Automation GmbH, Austria) in the back frame. The data of inertial measurement unit (IMU) are read through the RS-232 bus with a sample rate of 100Hz. The linear displacement sensors (LDS) placed in hip and knee joints, as well as 1D and 3D force sensors in the sole, are connected to AD converter with a sample rate of 1kHz. All data acquired by PLC are sent to PC in the real-time scale via EtherNet bus.

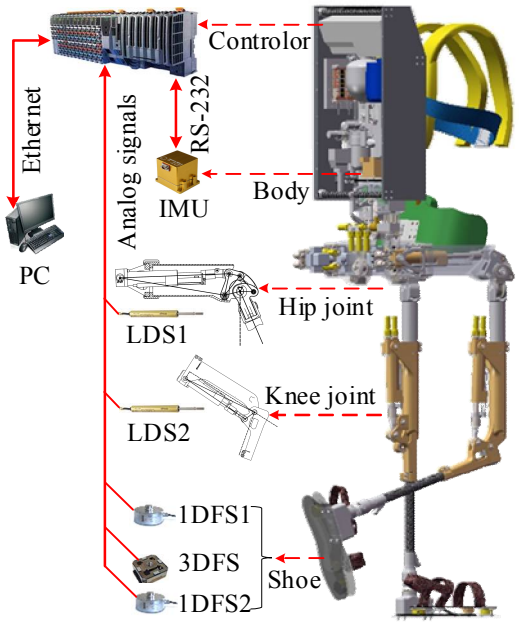

Figure 5. Hardware system of APAL

3.2. The trunk posture and acceleration of hip joints

To assess the trunk posture and acceleration of hip joints, a certain adaptation of IMU was required. Since it is fixed in the exoskeleton back frame, which is securely connected to the human trunk, the human trunk and exoskeleton postures are approximately the same in the sagittal plane, with disregard of minor wearing mismatch errors. As shown in Figure 6, the axis of IMU is set parallel to the body coordinate axis, and IMU can directly provide the attitude ${}^{W}\vec{\theta}_{IMU}=\{\theta_{roll},\ \theta_{pitch},\ \theta_{yaw}\}$ in the WCS, angular velocity ${}^{B}\vec{\dot{\theta}}_{IMU}=\{\omega_{roll},\omega_{pitch},\omega_{yaw}\}$, and acceleration ${}^{B}\vec{a}_{IMU}=\{{}^{B}\ddot{x}_{IMU},{}^{B}\ddot{y}_{IMU},{}^{B}\ddot{z}_{IMU}\}$ of IMU in the body coordinate system (BCS). The angular acceleration ${}^{B}\vec{\ddot{\theta}}_{IMU}$ of IMU in BCS can be obtained via the first-order difference of ${}^{B}\vec{\dot{\theta}}_{IMU}$. To improve the smoothness and reduce the high-frequency noise induced by quantization error, interpolation and low pass filter are used.

Preprints (www.preprints.org) | NOT PEER-REVIEWED | Posted: 11 June 2018 doi:10.20944/preprints201806.0149.v1

The acceleration ${}^{W}\ddot{x}_H$ ${}^{W}\ddot{z}_H$ of the hip joint in WCS cannot be measured directly by IMU because the two do not coincide, but they can be derived through kinematic relations. The acceleration ${}^{B}\vec{a}_{IMU}$ obtained by IMU is firstly converted from BCS to WCS as ${}^{W}\vec{a}_{IMU} = {}^{BtoW}R \cdot {}^{B}\vec{a}_{IMU}$, where ${}^{BtoW}R$ is the rotation matrix for BCS –WCS conversion. Let the coordinates of IMU in BCS be ${}^{B}\vec{P}_{IMU}$, and those in WCS be ${}^{W}\vec{P}_{IMU}$. Thus, the coordinate of the left hip joint in BCS is ${}^{B}\vec{P}_H$, and that in WCS should be ${}^{W}\vec{P}_H = {}^{BtoW}R \cdot ({}^{B}\vec{P}_H - {}^{B}\vec{P}_{IMU}) + {}^{W}\vec{P}_{IMU}$. The acceleration in WCS is ${}^{W}\vec{a}_H = {}^{W}\vec{P}_H{}'' = {}^{BtoW}R'' \cdot ({}^{B}\vec{P}_H - {}^{B}\vec{P}_{IMU}) + {}^{W}\vec{a}_{IMU}$. Here, ${}^{BtoW}R''$ is the second derivative of the rotation matrix ${}^{BtoW}R$. The required ${}^{W}\ddot{x}_H$ and ${}^{W}\ddot{z}_H$ are components of ${}^{W}\vec{a}_H$ on-axis x_W and z_W, respectively.

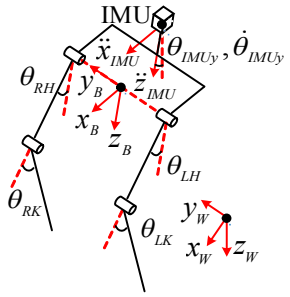

Figure 6. Trunk posture sensing with IMU and the limb attitude definition

3.3. The angles of hip and knee joints

The angle of human hip and knee joints are not measured directly but are derived from the respective measurements of the exoskeleton. The displacement signals s_H and s_K from LDSs are converted into hip and knee joint angles θ_H and θ_K, according to the geometry of the mechanical joints, as shown in Figure 7. The angular velocities $\dot{\theta}_H$ and $\dot{\theta}_K$ are obtained via the first-order differences of θ_H and θ_K. Similarly, the angular accelerations $\ddot{\theta}_H$ and $\ddot{\theta}_K$ are obtained from the first-order differential of $\dot{\theta}_H$ and $\dot{\theta}_K$.

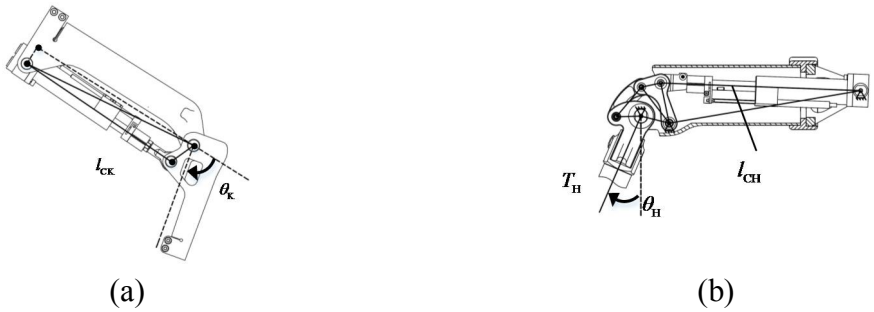

Figure 7. Exoskeleton joint geometry and angle measurements for (a) hip joint; (b) knee joint.

Figure 8 shows a group of actual curves constructed via in-situ running measurements. The stroke range of the linear displacement sensor is 0~73mm, corresponding to the knee joint angle range of 0~135°, and that of hip joint of -15~150°. We can see that for the in-situ running, the hip and knee joints' angles varied from 38° to 65° and from 60° to 100°, respectively. Thus, the hip and knee joints did not reach the stroke limit.

Preprints (www.preprints.org) | NOT PEER-REVIEWED | Posted: 11 June 2018 doi:10.20944/preprints201806.0149.v1

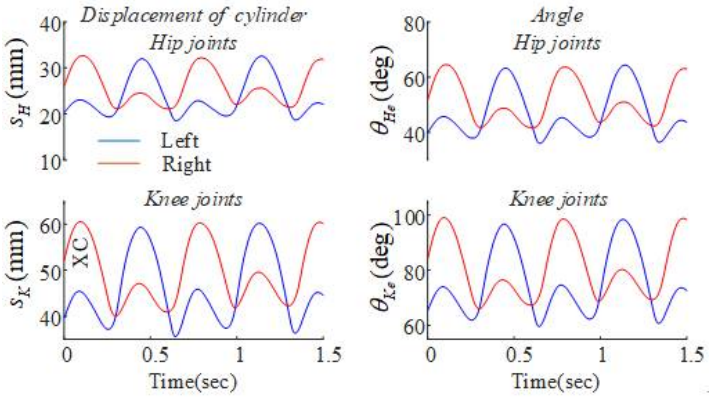

Figure 8. Joint information of exoskeleton robot, hip and knee cylinder displacement s_H , s_K ; hip and knee joint angle θ_H , θ_K

Next, based on the man-machine motion mapping, human hip and knee joint angle can be calculated. Since the exoskeleton knees are rigidly connected to human arches, while ankle axes of the exoskeleton and human body are nearly coaxial, the human ankle coordinates in BCS are nearly the same as those of the exoskeleton. This can be expressed as follows:

$$\begin{cases} x_F = l_{Te}\sin(\theta_{He}) - l_{Se}\sin(\theta_{Ke}-\theta_{He}) = l_T\sin(\theta_H) - l_S\sin(\theta_K-\theta_H) \\ z_F = l_{Te}\cos(\theta_{He}) + l_{Se}\cos(\theta_{Ke}-\theta_{He}) = l_T\cos(\theta_H) + l_S\cos(\theta_K-\theta_H) \end{cases} \tag{7}$$

where θ_{He} and θ_{Ke} are hip and knee joint angles of the exoskeleton; l_{Te} and l_{Se} are lengths of thigh and shank of exoskeletons, which are 450 and 440 mm, respectively; l_T and l_S are lengths of components T and S of the simplified human model, which are 424 and 422 mm, respectively. Equation 7 allows one to derive joint angles of the human body θ_H and θ_K, as well as $\dot{\theta}_H$, $\dot{\theta}_K$, $\ddot{\theta}_H$, and $\ddot{\theta}_K$, as shown in Figure 9.

Here we manually adjust the thigh and shanks length of the exoskeleton to be slightly smaller than those of the wearer. When the wearer stands straight, the exoskeleton is slightly squatting. This helps to avoid the dead point when the knee joint approaches 0 degrees and does not affect the motion mapping. The results obtained show that the human knee joint angle is 16-53°, the angular velocity is about -300-300°/s, the angular acceleration is -3500-15400°/s², and the hip joint is -15~81°, the angular velocity is about -540~545°/s, and the angular acceleration is -5700-27000°/s². It can be seen that the joint angular velocity obtained from the numerical difference is relatively smooth, but the angular acceleration exhibits a sharp variation caused by a touchdown impact.

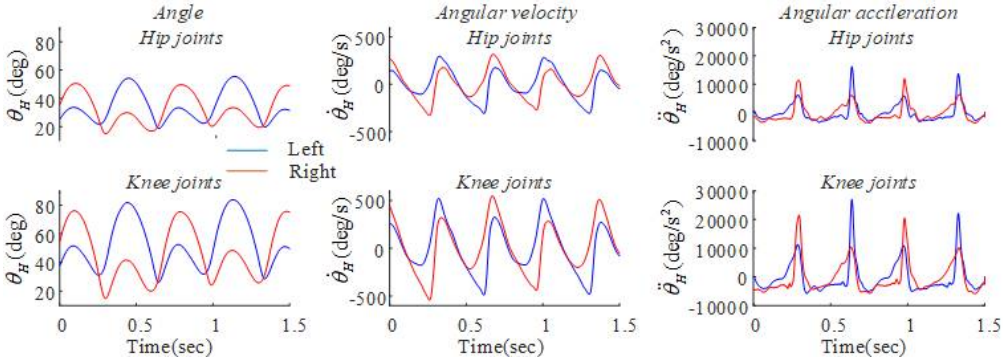

Figure 9. Joint information of human lower limbs, hip and knee angle, angular velocity, and angular acceleration

Preprints (www.preprints.org) | NOT PEER-REVIEWED | Posted: 11 June 2018 doi:10.20944/preprints201806.0149.v1

3.4. Foot contact forces (FCFs)

A special shoe is developed to measure FCF in the sagittal plane. There are three components of FCF, which include F_{Fx} in the front-rear direction, F_{Fz} in the up-down direction, and torque T_{Fy} on the dorsiflexion axis. The force condition of the sole is complex. On the one hand, there are many contact states on the sole during exercise, such as heel strike, full foot landing, forefoot landing, and toe landing, etc., while the ground unevenness can also cause unpredictable deformation of the sole. On the other hand, the rotational freedom of the human toe joint is required for walking stability and energy saving [24], so the sole should be flexible. Thus, the double-layer elastic steel sole structure was designed, as shown in Figure 10.

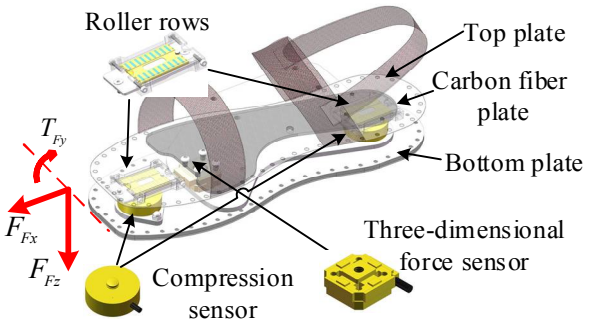

Figure 10. Foot force measurement device.

The upper steel plate is connected to the human foot, while the lower steel plate is connected to the exoskeleton, and three force sensors couple by the two layers. Under the arch, a solid carbon fiber plate is used to reinforce the flexible steel plate to increase its stiffness, which forms a strong support for the arch, while the area under the toe joint is not provided with a carbon fiber plate. When the toe joint rotates, the upper and lower two layers of elastic steel plate can follow the plantar deformation.

Regarding the choice of sensor placement, both the single- and multi-sensor solutions have been used. Authors [25] introduced an integrative force sensor dedicated to FCF measurement, which combines high integration with high accuracy. However, the sensor should be strong enough to withstand large torque during heel/ toe landing, which will increase the size and weight of the sensor. Meanwhile, the sole is usually set as a rigid body to avoid any damage induced by the local distortion. This prevents the toe joint from bending, which deteriorates the wear comfort. This makes the multi-sensor solution more preferable [26], since the footplate bears a smaller bending torque and can be made lighter and thinner. However, the internal stress is easily generated between the sensors, causing zero drift and other errors.

The proposed design is a combination of one 3D force sensor and two 1D force sensors. A 1D force sensor with a high overload margin is set under the heel to measure GRF F_{z1} on the heel. This sensor can directly withstand the large impact load during the heel strike. A 3D force sensor is arranged slightly behind the toe joint, and the sensor can obtain up-down direction force F_{z2} and front-rear direction force F_{x2}. After the heel is off the ground, the toe joint begins to bend, and the pressure center is transferred to the toe. A 1D force sensor is placed under the toe to measure the supporting force F_{z3}. The sensor layout and force analysis model are shown in Figure 11. When using multiple force sensors to measure the same object at the same time, if there is an over-constraint in the mounting structure, it is likely to cause internal stress and zero-drift errors. Hence, a special treatment of the force sensor connector is performed. The bottom of 3D force sensors is fixed to the lower elastic steel plate, while the upper end is connected with the upper plate through a 1DOF hinge, releasing the constraint of the vertical axial rotation. Two 1D force sensors are connected to the upper plate through a spherical hinge with three DOFs and a sliding pair with one DOF. Thus, the 1D force sensor bears only the axial tensile and lateral forces, in order to avoid the disturbance of the front-

Preprints (www.preprints.org) | NOT PEER-REVIEWED | Posted: 11 June 2018 doi:10.20944/preprints201806.0149.v1

rear direction horizontal force measurement. The sliding pair on the 1D force sensor under the toe has a long slide. When the toe joint bends, the upper and lower layers of elastic steel plates will be subjected to pressure. The needle roller rows will roll along the slide to prevent the motion interference and ensure the activity degree of the toe joint.

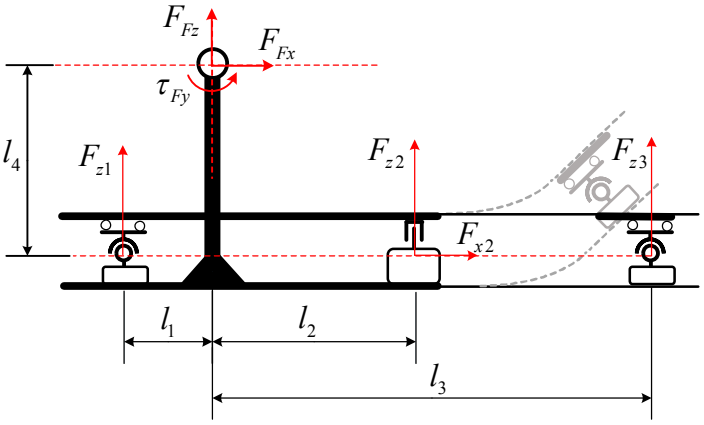

Figure 11. Synthesis of multiple force sensor signals on the sole.

For computational purposes, we synthesize the force signals obtained from the force sensors at the ankle joint. The resultant forces can be calculated based on the location of the force sensors.

$$\begin{cases} F_{Fx} = F_{x2} \\ F_{Fz} = F_{z1} + F_{z2} + F_{z3} \\ \tau_{Fy} = F_{x2}l_4 - F_{z1}l_1 + F_{z2}l_2 + F_{z3}l_3 \end{cases} \tag{8}$$

Signals from the sensor and the resultant force are shown in Figure 12. One can see that during in-situ running, the toe first touches the ground, so the force F_{z3} from the force sensor below the toe is firstly generated. When F_{z1} from the force sensor below the heel is generated, this indicates that the entire foot is on the ground. The following is the push-off process. One can see that the resultant force in the vertical direction is significantly higher than the wearer's gravity force, pushing the body to accelerate upwards and leap. Until the overall toe force drops to zero, the foot leaves the ground and switches to the swing phase. At this stage, FCF should be zero, but the exoskeleton robot power system is not turned on during the experiment, so the wearer needs to bear a part of the exoskeleton leg weight. Therefore, the foot force in the vertical direction during the swing phase is negative. This demonstrated that the foot force-measuring device is more adaptable to different contact states of a foot and can reliably measure the human foot contact force in both support and swing phases.

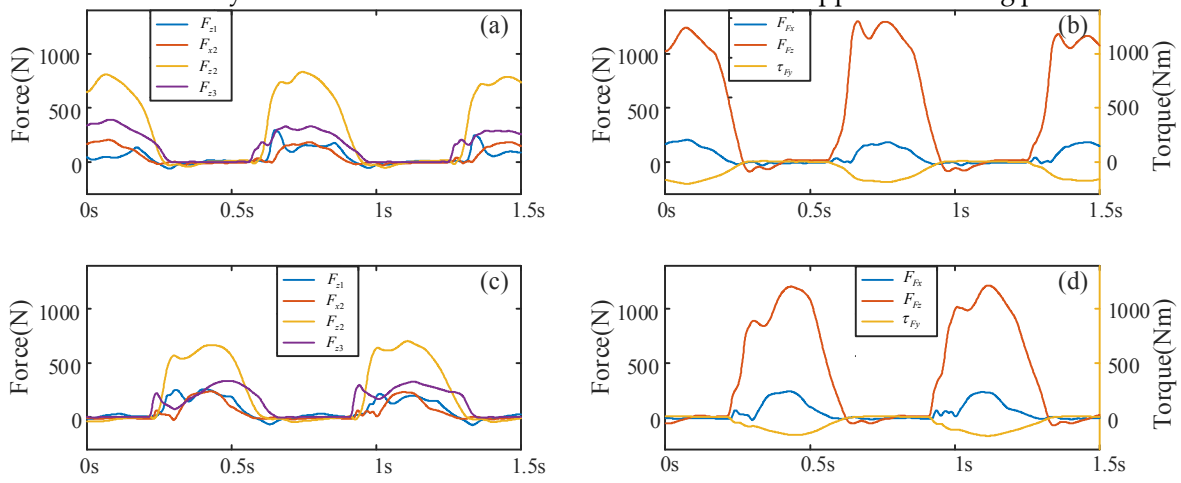

Preprints (www.preprints.org) | NOT PEER-REVIEWED | Posted: 11 June 2018 doi:10.20944/preprints201806.0149.v1

Figure 12. (a) Force signals from each sensor on the left foot; **(b)** resultant force signals on the left foot; **(c)** force signals from each sensor on the right foot; **(d)** resultant force signals on the right foot.

3.5. Human joint torque solution

Using the above sensing system, all parameters required for solving the human inverse dynamics equation are obtained. The mass-induced torques at hip and knee joints τ_{T1} and τ_{S1} can be obtained via Equation 4, as shown in Figure 13(a). The FCF-induced torques τ_{T2} and τ_{S2} can be derived via Equation 5, as shown in Figure 13(b). The resultant joint torque τ_T is calculated via Equation 6, as shown in Figure 13(c). So far, the human joint torque calculation is accomplished. From the results, we can see that in the support phase, the FCF-induced joint torque is far higher than the mass-induced one. According to Equation 5, FCF and the joint angles have a more significant influence on the result. In the swing phase, the foot contact force is small, and the mass-induced joint torque becomes the main component. According to Equation 4, the inertial parameters of human limbs, the acceleration at hip joints, and the joint angle, angular velocity, and angular acceleration exert a strong effect on the results.

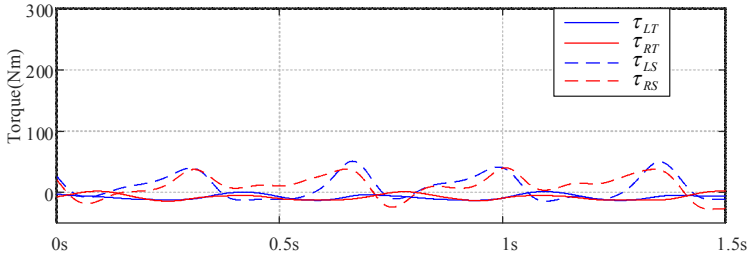

(a) Torques of hip and knee joints induced by the mass force

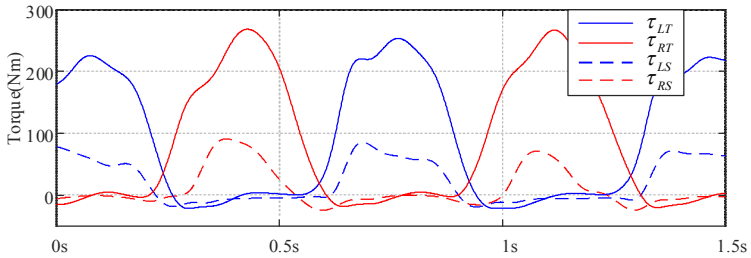

(b) Torques of hip and knee joint induced by the foot contact force

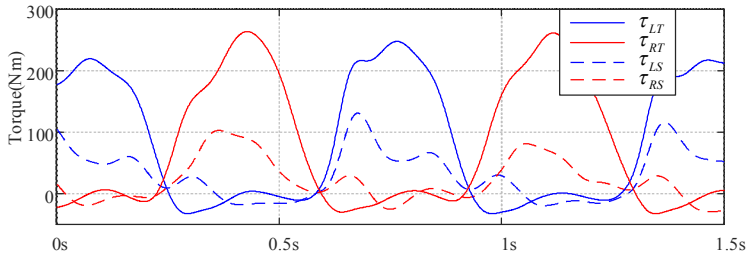

(c) Combined torque of the hip and knee joint torques

Figure 13. Human joint torque calculated from in-situ running

4. Contrast experiments

To verify the overall accuracy of the human joint torque derived from the integrated sensor system of the exoskeleton robot and the proposed IDA equations, we used the commercial motion capture system developed by Motion Analysis Corporation (USA) to synchronously obtain the body's motion data and joint torque, as shown in Figure 14.

Preprints (www.preprints.org) | NOT PEER-REVIEWED | Posted: 11 June 2018 doi:10.20944/preprints201806.0149.v1

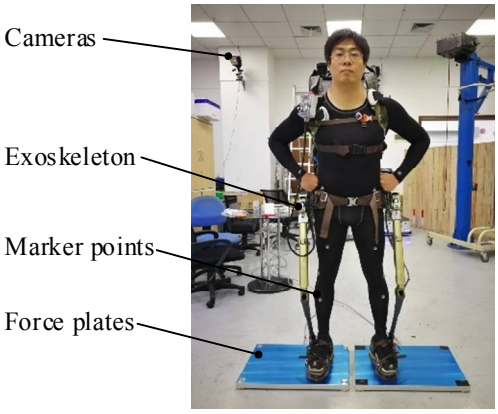

Figure 14. Experiment environment.

Two evaluation indicators are used. The first one is the root mean square error (RMSE), which can quantitatively evaluate the calculation error.

$$RMSE = \sqrt{\frac{\sum_{k=1}^{N}[\tau_{EXOk} - \tau_{MAk}]^2}{N}} \tag{9}$$

The second one is the correlation coefficient R, which reflects the similarity between two curves.

$$R = \frac{\sum_{k=1}^{n}\tau_{EXOk}\cdot\tau_{MAk} + \frac{1}{n}\left(\sum_{k=1}^{n}\tau_{EXOk}\right)\cdot\left(\sum_{k=1}^{n}\tau_{MAk}\right)}{\sqrt{\sum_{k=1}^{n}\tau_{EXOk}^{\ 2} - \frac{1}{n}\left(\sum_{k=1}^{n}\tau_{EXOk}\right)^2}\sqrt{\sum_{k=1}^{n}\tau_{MAk}^{\ 2} - \frac{1}{n}\left(\sum_{k=1}^{n}\tau_{MAk}\right)^2}} \tag{10}$$

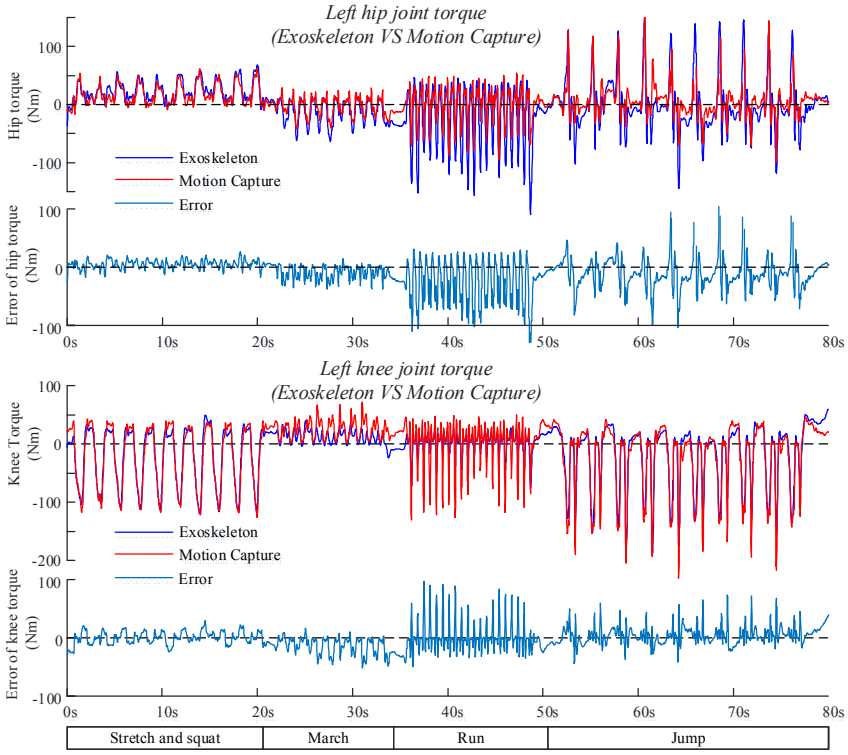

Figure 15. Comparison of two torque outputs of left leg from the motion capture system and the exoskeleton robot.

Preprints (www.preprints.org) | NOT PEER-REVIEWED | Posted: 11 June 2018 doi:10.20944/preprints201806.0149.v1

According to the instructions of the motion capture system, the wearer pastes the marker points to his/her body, connects the exoskeleton robot, and performs squatting, walking, running and jumping exercises in sequence on the force plate of the motion capture system for 10, 20, and 10 times, respectively. The motion capture system and the exoskeleton robot system collect data simultaneously, and the joint torques of the left and right legs of the human body are calculated, as shown in Figures 15 and 16.

Among four actions: squatting, walking, running, and jumping, each action is repeated for ten times, and the statistical results obtained are shown in Table 2.

Table 2. RMSE (*E*) and correlation coefficient (*R*) for two outputs from different limb joints in different gaits for the left leg.

Sub	Squatting				Walking				Running				Jumping			
	Hip		Knee		Hip		Knee		Hip		Knee		Hip		Knee	
	E	R	E	R	E	R	E	R	E	R	E	R	E	R	E	R
G 1	7.1	0.93	9.8	0.96	17.1	0.75	8.8	0.66	52.5	0.77	22.7	0.93	29.7	0.81	14.7	0.97
G 2	7.8	0.74	8.2	0.99	14.2	0.88	11	0.81	58.8	0.89	15.1	0.81	18.6	0.87	13.2	0.97
G 3	10.7	0.81	9	0.98	13.5	0.88	10.1	0.71	37.1	0.69	30.2	0.94	25.5	0.85	12.5	0.98
G 4	9.2	0.92	7.6	0.99	17.3	0.85	19.8	0.62	37.5	0.75	29.3	0.85	31.3	0.83	11.1	0.98
G 5	9.4	0.9	6.9	0.99	19.9	0.9	20.7	0.07	39.5	0.67	23.8	0.93	54.8	0.31	15.8	0.97
G 6	8.3	0.95	11.4	0.98	11	0.64	13	0.84	36.5	0.78	27.9	0.87	76.2	-0.4	12.2	0.97
G 7	8.9	0.94	8.1	0.99	12.2	0.89	14.8	0.71	39.7	0.78	23	0.91	54.4	0.15	16.2	0.97
G 8	9.5	0.9	9.3	0.99	12.3	0.84	23.1	0.43	36.8	0.77	28.9	0.94	68.1	-0.3	13.8	0.98
G 9	10.1	0.93	10.5	0.98	13.7	0.76	16.5	0.41	47.4	0.85	18.4	0.92	20.9	0.94	15.3	0.97
G 10	10.4	0.95	6.7	0.99	13.1	0.87	21.5	0	51.7	0.83	17.6	0.88	63.4	-0.3	10.9	0.98
Mean	9.14	0.9	8.75	0.98	14.4	0.83	**15.9**	**0.53**	43.8	0.78	23.7	0.9	**44.3**	**0.38**	13.6	0.97
SD	1.15	0.07	1.54	0.01	2.78	0.08	**5.16**	**0.29**	8.15	0.07	5.36	0.04	**21.4**	**0.55**	1.9	0.01

At the squatting stage, the hip and knee joint data exhibit a good fit. The mean RMSE is less than 10 Nm, and the correlation coefficient exceeds 0.9, indicating a high similarity of the waveforms.

At the walking stage, the matching degree of the knee joint data is significantly reduced, and the correlation coefficient even becomes negative at times. This may be attributed to the fact that the knee joint at the walking stage is almost straight and stays at the dead point support state, so the torque is small at this time, while the relative interference from each link of the system is relatively large. The hip joint at the walking stage mainly controls the trunk attitude, while the torque is significant, and the error is relatively small.

At the running stage, the hip and knee joint torques are significantly higher than those at the walking stage, so the corresponding RMSE is significantly increased, but the waveform similarity is better than that at the walking stage. This phenomenon strongly indicates that the proposed IDA process is similar to that of the motion capture system, but the difference mainly lies in the model of human body. After wearing the exoskeleton robot, the marker point that should be placed behind the pelvis of the wearer can only be moved onto the exoskeleton. Otherwise, it will be covered by the exoskeleton. This unavoidable defect will cause artificial changes to the model of the human body and deteriorate the final result.

At the jumping stage, the joint torque is significantly higher than that at other stages. The RMSE of the hip joint is slightly higher than that of the running stage, but the correlation coefficient is reduced. This implies that the pulse load and high-speed balancing adjustment make the hip joint torque fluctuate rapidly, thereby, reducing the waveform similarity. However, there is no significant increase in the RMSE when the torque is significantly raised, indicating that when the joint torque of the human body is large, the relative error is likely to be reduced. The knee joint data further confirm this trend. At the same time, although the torque of the knee joint is large, low RMSE (13.6 Nm) and high *R* (0.97) indicate that the knee joint error is minimal. This allows one to assume that FCF-induced

Preprints (www.preprints.org) | NOT PEER-REVIEWED | Posted: 11 June 2018 doi:10.20944/preprints201806.0149.v1

torque is significantly higher than the mass-induced component. The FCF component is controlled by the measurement accuracy of FCF and attitude angle, being less affected by the disturbance induced by the inertial acceleration, joint angular velocity, and angular acceleration derived by the multi-order differential. Therefore, it is easier to obtain a high precision, which is also confirmed by the results obtained at squatting and running stages.

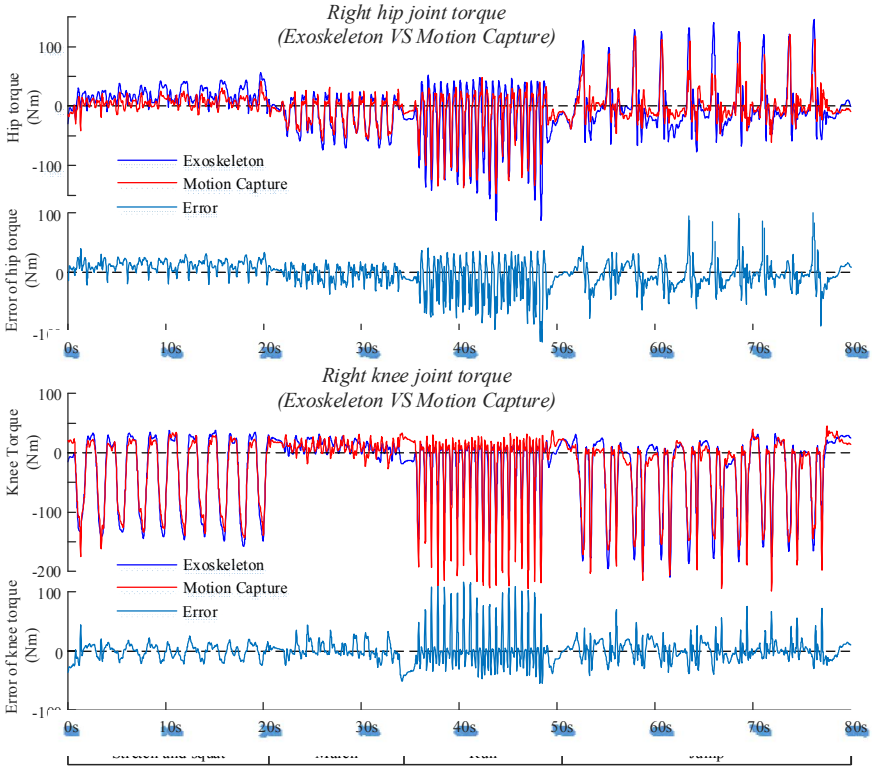

Figure 16. Comparison of two torque outputs of right leg from the motion analysis system and the exoskeleton robot.

Table 3. RMSE (E) and correlation coefficient (R) for two outputs from different limb joints in different gaits for the right leg.

Sub	Squatting				Walking				Running				Jumping			
	Hip		Knee		Hip		Knee		Hip		Knee		Hip		Knee	
	E	R	E	R	E	R	E	R	E	R	E	R	E	R	E	R
G 1	17.9	0.72	12.9	0.94	11.5	0.85	8.6	0.42	23.8	0.91	17	0.98	24.9	0.87	15.2	0.97
G 2	13.5	0.19	8.6	0.99	13.8	0.92	11.3	-0.2	41.3	0.89	23.1	0.95	16.1	0.85	16.3	0.96
G 3	15.4	0.59	7.5	1	10.5	0.91	15	-0.1	38.9	0.87	33.5	0.95	19.9	0.92	15.2	0.97
G 4	15.3	0.44	8.5	1	15.7	0.92	8.5	0.57	27.4	0.89	37	0.97	21.9	0.93	11.1	0.99
G 5	14.9	0.77	9.7	1	14.5	0.92	10.5	0.15	33.5	0.83	33.5	0.96	51.8	0.21	15.3	0.97
G 6	15	0.66	8.7	0.99	14.5	0.95	5.8	0.65	29.3	0.86	31.8	0.96	78.2	-0.5	15.4	0.96
G 7	16.1	0.59	10.4	0.99	9.8	0.91	12.7	-0.1	35.6	0.87	31.4	0.96	48	0.29	13.9	0.97
G 8	15	0.8	9.9	1	10.3	0.93	13.3	-0.1	31.7	0.87	35.2	0.96	57.5	-0.1	13.5	0.98
G 9	15.1	0.69	9.3	0.99	13.2	0.92	11.7	0.46	33.3	0.88	36.8	0.94	15.5	0.93	12.3	0.97
G 10	17.5	0.79	11	1	14	0.92	12.5	0.17	39.4	0.87	29.9	0.95	70	-0.2	17	0.96
Mean	15.6	**0.62**	9.65	0.99	12.8	0.92	**11**	**0.2**	33.4	0.87	30.9	0.96	**40.4**	**0.42**	14.5	0.97
SD	1.3	0.19	1.53	0.02	2.08	0.03	**2.71**	**0.31**	5.59	0.02	6.33	0.01	**23.6**	**0.55**	1.82	0.01

The data on the right leg at each stage is similar to that of the left leg, but the overall error is larger than that of the left leg. It was experimentally proved that the data on left and right legs are not entirely symmetrical. Notably, during the running stage, the torque of the right knee joint is significantly larger than that of the left knee. We repeatedly performed multiple tests and carefully checked possible errors in each link of the system, but this phenomenon still manifested itself. This can be attributed to certain differences in the strength and flexibility of left and right legs of the experimenter. Other possible causes of experimental errors are listed in Appendix B.

In general, the joint torque measurement method proposed in this study has favorable consistency with the motion capture system, in case of smooth motion with large joint torques, confirmed the feasibility of the proposed system design and theory. The exoskeleton APAL robot furnishes the real-time provision of the human joint torque based on its integrated sensor system. It also achieves the goal of active power-assistance, which principle was described in Section 2.3.

5. Conclusions

This paper studied a new approach to the human body motion intention estimation for active power-assist lower limb exoskeleton robot (APAL). The following conclusions can be drawn from this study. Through analyzing the conduction and manifestations of motion intention of the human body at different stages we confirmed that the muscular torque proportional compensation (MTPC) is a general and effective mechanism for realizing the active power-assist function. The joint torque of human body is chosen as the motion intention indicator because it meets the requirements to active power-assist MIE, namely: (i) it reflects the direction and intensity of the wearer's efforts; (ii) it precedes the human limb motion; (iii) it generates real-time and continuous output. An active power-assist mechanism was set up, and the effort of MTPC was briefly verified. To calculate the human joint torque, an online calculation method was proposed based on the inverse dynamics approach (IDA) with the dynamic model of human body, and the sensing system integrated into an exoskeleton robot (APAL) was designed to perceive the motion data and foot contact force of the human body. Finally, contrast experiments were carried out with the motion capture system. Root mean square error (RMSE) and correlation coefficient R were employed to evaluate the accuracy and similarity. Comparison of two synchronous results shows a good accuracy of the proposed MIE method, which lays the foundation for the realization of active power-assist.

The advantages of the proposed method are as follows.

(1) There is no need to measure biological signals such as EMG, and no external auxiliary system is required for its practical application.
(2) It is not necessary to distinguish the gait type, and it is not even necessary to distinguish the support or swing phases, so that MIE of arbitrary human motion can be realized.
(3) The output is a real-time and continuous joint torque curve that can be directly used for the joint motion control of exoskeleton robots.

Acknowledgments: This work is supported by Shenzhen Peacock Plan (KQTD2016112515134654), National Natural Science Foundation of China (U1713222, No.61773139 and No.61473015), and Natural Science Foundation of Heilongjiang Province, China (Grant No.F2015008).

Author Contributions: J.D. conceived the method and wrote the paper; M.L. and F.Z. helped to modify it; S.Q. performed the experiments and analyzed the data; X.W. contributed theoretical justification and reference materials. All authors have read and approved the final manuscript.

Conflicts of Interest: The authors declare no conflict of interest.

Appendix A

First, determine the coordinates of the center of mass of component T in the global coordinate system O_W .

 doi:10.20944/preprints201806.0149.v1

$$\begin{cases} x_{CT} = x_H + l_{CT}\sin(\theta_T) \\ z_{CT} = z_H + l_{CT}\cos(\theta_T) \end{cases} \tag{11}$$

Next, derive the motion velocity of the center of mass of component *T*.

$$\begin{cases} \dot{x}_{CT} = \dfrac{\partial x_{CT}}{\partial x_H}\dot{x}_H + \dfrac{\partial x_{CT}}{\partial \theta_T}\dot{\theta}_T \\ \dot{z}_{CT} = \dfrac{\partial z_{CT}}{\partial z_H}\dot{z}_H + \dfrac{\partial z_{CT}}{\partial \theta_T}\dot{\theta}_T \end{cases} \tag{12}$$

Then, calculate the coordinates of the center of mass of component *S* in the global coordinate system O_W.

$$\begin{cases} x_{CS} = x_H + l_T\sin(\theta_T) + l_{CS}\sin(\theta_S) \\ z_{CS} = z_H + l_T\cos(\theta_T) + l_{CS}\cos(\theta_S) \end{cases} \tag{13}$$

Next, derive the motion velocity of the center of mass of component *S*

$$\begin{cases} \dot{x}_{CS} = \dfrac{\partial x_{CS}}{\partial x_H}\dot{x}_H + \dfrac{\partial x_{CS}}{\partial \theta_T}\dot{\theta}_T + \dfrac{\partial x_{CS}}{\partial \theta_S}\dot{\theta}_S \\ \dot{z}_{CS} = \dfrac{\partial z_{CS}}{\partial z_H}\dot{z}_H + \dfrac{\partial z_{CS}}{\partial \theta_T}\dot{\theta}_T + \dfrac{\partial z_{CS}}{\partial \theta_S}\dot{\theta}_S \end{cases} \tag{14}$$

Thereby, calculate the total kinetic energy of the system

$$K = \frac{1}{2}\left[m_T(\dot{x}_{CT}^{\ 2} + \dot{z}_{CT}^{\ 2}) + m_S(\dot{x}_{CS}^{\ 2} + \dot{z}_{CS}^{\ 2}) + I_T\dot{\theta}_T^{\ 2} + I_S\dot{\theta}_S^{\ 2} \right] \tag{15}$$

Then, the total kinetic energy of the system is derived as follows

$$P = -m_T g z_T - m_S g z_S \tag{16}$$

Appendix B

There are many links in the experiment that may cause errors, which are summarized as follows.

1) The errors in the human body model induced by simplification and individual differences are difficult to avoid.
2) Sensor errors, including foot sensors, IMUs, displacement sensors, and others. It is particularly challenging to deal with temperature drift, zero drift, and similar factors.
3) Data errors in the motion capture system, such as misplacement of the marker point on the knee joint by 10mm forward and backwards, can cause the knee joint torque fluctuations of about 20%.
4) Exoskeleton wearing mismatch errors, exoskeleton design, and the human coordinate system exhibit a relatively accurate and stable positional relationship, which issue needs further in-depth consideration.
5) On the one hand, calculation errors studied in this paper are limited to the sagittal plane dynamics. The coupling terms of the frontal and coronal plane motions also cause differences in two datasets. On the other hand, the sampling delays, interpolations, and filters involved in the program can cause differences in the respective curves.

References

1. Esquenazi, A.; Talaty, M.; Packel, A.; Saulino, M. The ReWalk powered exoskeleton to restore ambulatory function to individuals with thoracic-level motor-complete spinal cord injury. *Am J Phys Med Rehabil* **2012**, 91, 911-921.
2. Pransky, J. The Pransky interview: Russ Angold, Co-Founder and President of Ekso™ Labs. *Industrial Robot* **2014**, 41, 329.
3. Preusche, C.; Ortmaier, T.; Hirzinger, G. Teleoperation concepts in minimal invasive surgery. *Control Engineering Practice 2002*, 10, 1245-1250.
4. Kazerooni, H.; Steger, R. That which does not stabilize, will only make us stronger. *International Journal of Robotics Research* **2007**, 26, 75-89.
5. Ghan, J.; Kazerooni, H. System identification for the Berkeley lower extremity exoskeleton (BLEEX). In Proceedings of the 2006 International Conference on Robotics and Automation, Orlando, FL, USA, 15-19 May 2006; pp. 3477-3484.
6. Song, Z.; Guo, S.; Nan, X.; Gao B.; Shi, L. Implementation of human-machine synchronization control for active rehabilitation using an inertia sensor. *Sensors* **2012**, 12, 16046-16059.
7. Ka, D.M.; Hong, C.; Toan, T.H.; Qiu, J. Minimizing human-exoskeleton interaction force by using global fast sliding mode control. *International Journal of Control Automation & Systems* **2016**, 14, 1-10.
8. Jin, X.; Zhu, S.; Zhu, X.; Chen Q.; Zhang X. Single-input adaptive fuzzy sliding mode control of the lower extremity exoskeleton based on human-robot interaction. *Advances in Mechanical Engineering* **2017**, 9, 1-9.
9. Zhang, C.; Zang, X.; Leng Z.; Yu, H.; Zhao, J.; Zhu, Y. Human-machine force interaction design and control for the HIT load-carrying exoskeleton. *Advances in Mechanical Engineering* **2016**, 8, 1-14.
10. Kawamoto, H.; Sankai, Y. Power assist method based on phase sequence and muscle force condition for HAL. *Advanced Robotics* **2005**, 19, 717-734.
11. Lloyd, D.G.; Besier, T.F. An EMG-driven musculoskeletal model to estimate muscle forces and knee joint moments in vivo. *Journal of Biomechanics* **2003**, 36, 765-776.
12. Krasin, V.; Gandhi, V.; Yang, Z.; Karamanoglu, M. EMG based elbow joint powered exoskeleton for biceps brachii strength augmentation. In Proceedings of the 2015 International Joint Conference on Neural Networks, Killarney, Ireland, 1 October 2015; pp. 1-6.
13. Peternel, L.; Noda, T.; Petrič, T.; Ude, A.; Morimoto, J.; Babič1, J. Adaptive control of exoskeleton robots for periodic assistive behaviours based on EMG feedback minimisation. *Plos One* **2016,** 11, 1-26.
14. Han, H.; Han, H.; Kim, J. Development of real-time muscle stiffness sensor based on resonance frequency for physical human-robot interactions. In Proceedings of the Annual International Conference of the IEEE Engineering in Medicine and Biology Society, San Diego, California, USA, August 28-September 1, 2012; pp. 2367-2370.
15. Hoy, M.G.; Zajac, F.E.; Gordon, M.E. A musculoskeletal model of the human lower extremity: the effect of muscle, tendon, and moment arm on the moment-angle relationship of musculotendon actuators at the hip, knee, and ankle. *Journal of Biomechanics* **1990**, 23, 157-169.
16. Taube, W.; Leukel, C.; Gollhofer, A. How neurons make us jump: the neural control of stretch-shortening cycle movements. *Exercise & Sport Sciences Reviews* **2012**, 40, 106-115.
17. Dawson, G.D. The relative excitability and conduction velocity of sensory and motor nerve fibres in man. *J. Physiol*. **1956**, 131, 436–451.
18. Fitzpatrick, R.C.; Gorman, R.B.; Burke, D.; Gandevia S. Postural proprioceptive reflexes in standing human subjects: bandwidth of response and transmission characteristics. *Journal of Physiology* **1992**, 458, 69-83.
19. Robertson, B.D.; Farris. D.J.; and Sawicki, G.S. More is not always better: modeling the effects of elastic exoskeleton compliance on underlying ankle muscle-tendon dynamics. *Bioinspiration & Biomimetics* **2014**, 9, 1-11.

 doi:10.20944/preprints201806.0149.v1

20. Camomilla, V.; Cereatti, A.; Cutti, A.G.; Fantozzi S.; Stagni R.; Vannozzi G. Methodological factors affecting joint moments estimation in clinical gait analysis: a systematic review. *Biomedical Engineering Online* **2017**, 16, 2-27.
21. Karatsidis, A.; Bellusci, G.; Schepers, M.; Zee M.D.; Andersen M.S.; Veltink P.H. Estimation of ground reaction forces and moments during gait using only inertial motion capture. *Sensors* **2017**, 17, 1-22.
22. Wu, J.; Wang, Q.; Fan, J.; Zhou J. The method of feature-based parametric mannequin modeling. *Journal of Huazhong University of Science and Technology* **2000**, 28, 29-32.
23. Deng, J.; Wang, P.; Li, M.; Guo, W.; Zha, F.; Wang, X. Structure design of active power-assist lower limb exoskeleton APAL robot. *Advances in Mechanical Engineering* **2017**, 9, 1-11.
24. Wang, Q.; Wang, L.; Zhu, J. Effects of toe stiffness on ankle kinetics in a robotic transtibial prosthesis during level-ground walking. *Mechatronics* **2014**, 24, 1254-1261.
25. Son, B.J.; Baek, Y.S.; Kim, J.H. Development of foot modules of an exoskeleton equipped with multiple sensors for detecting walking phase and intent. *Applied Mechanics & Materials* **2015**, 752-753, 1016-1021.
26. Bamberg, S.J.; Benbasat, A.Y.; Scarborough, D.M.; Krebs D.E.; Paradiso J.A. Gait analysis using a shoe-integrated wireless sensor system. *IEEE Transactions on Information Technology in Biomedicine* **2008**, 12, 413-423.